

Full paper

Interfacial engineering for stabilizing polymer electrolytes with 4V cathodes in lithium metal batteries at elevated temperature

Zeyuan Li^{a,1}, Aijun Li^{a,b,1}, Hanrui Zhang^{a,1}, Ruqian Lin^c, Tianwei Jin^a, Qian Cheng^a, Xianghui Xiao^d, Wah-Keat Lee^d, Mingyuan Ge^d, Haijun Zhang^{e,**}, Amirali Zangiabadi^a, Iradwikanari Waluyo^d, Adrian Hunt^d, Haowei Zhai^a, James Joseph Borovilas^a, Peiyu Wang^a, Xiao-Qing Yang^c, Xiuyun Chuan^b, Yuan Yang^{a,*}

^a Program of Materials Science and Engineering, Department of Applied Physics and Applied Mathematics, Columbia University, New York, NY, 10027, United States

^b Key Laboratory of Orogenic Belts and Crustal Evolution, School of Earth and Space Sciences, Peking University, Beijing, 100871, China

^c Chemistry Division, Brookhaven National Laboratory, Upton, NY, 11973, United States

^d National Synchrotron Light Source II, Brookhaven National Laboratory, Upton, NY, 11973, United States

^e Beijing Innovation Center for Materials Genome Engineering, University of Science and Technology Beijing, 10083, China

ARTICLE INFO

Keywords:

Lithium metal batteries
Surface passivation
Poly (ethylene oxide)
High-voltage cathode
Energy density

ABSTRACT

Poly (ethylene oxide) (PEO) polymer electrolytes are promising candidates for next-generation rechargeable lithium batteries. However, the poor interfacial stability between 4 V cathodes and PEO electrolytes impedes their applications in 4 V lithium batteries with high energy density. Here, we demonstrate a facile and effective strategy to enhance the interfacial stability by the synergy of $\text{Li}_{1.5}\text{Al}_{0.5}\text{Ge}_{1.5}(\text{PO}_4)_3$ (LAGP) coating on the cathode surface, and salt combination in the electrolyte, even with a cut-off voltage of 4.25–4.4 V vs. Li^+/Li . Nano-LAGP coated $\text{Li}|\text{PEO}|\text{LiCoO}_2$ cell delivers stable cycling with a capacity retention of 81.9%/400 cycles and 84.7%/200 cycles at 60 °C when charged to 4.25 and 4.3 V in pure polyether electrolyte, respectively. Steady cycling is also demonstrated at room temperature and with $\text{LiNi}_{0.5}\text{Co}_{0.2}\text{Mn}_{0.3}\text{O}_2$ (NCM523) cathode. This work offers a viable and scalable approach to improve the stability between PEO electrolytes and 4 V cathodes and open up new possibilities for practical application of 4 V lithium metal batteries.

1. Introduction

With the fast-growing demands of portable electronics, electric vehicles and grid-level energy storage, lithium batteries with high energy density are urgently needed [1–8]. To achieve high energy density, significant developments of cathode materials (e.g. LiCoO_2 (LCO), Ni-rich $\text{Li}(\text{Ni}_{x}\text{Co}_{y}\text{Mn}_{1-x-y})\text{O}_2$ (NCM) and $\text{LiNi}_{1-x-y}\text{Co}_x\text{Al}_y\text{O}_2$ (NCA)) with high capacity and high voltage, as well as anodes with high capacity (e.g. lithium metal) are essential [9–12]. Along with the pursuit of high energy density, safety is also critical to avoiding thermal runaway and catastrophic failures in batteries [13–15]. In this regard, polymer electrolytes are promising solutions since they are scalable in manufacturing and have a much higher flash point (>150–200 °C) [16–18] compared to conventional flammable liquid electrolytes (~25 °C) [19], which can

significantly improve the thermal stability of batteries.

Among various polymer electrolytes, poly (ethylene oxide) (PEO) electrolytes have gained widespread interests because of their low cost and easiness to process [13,20,21]. More importantly, PEO electrolytes have been reported to be chemically compatible with lithium metal [22,23], which makes them more attractive than carbonate electrolytes in lithium metal batteries [24,25]. Electric vehicle “Bluecars” equipped with Li-metal|PEO| LiFePO_4 (LFP) battery has been commercialized by Bolloré. However, they need to be operated at 70–80 °C and has limited specific energy of 100 Wh kg⁻¹ at the system level [26]. Replacing LFP by 4 V cathodes, such as LCO and NCM, can remarkably enhance specific energy. Unfortunately, PEO degrades fast above 4 V vs. Li^+/Li due to its rapid oxidation [27–29], which substantially deteriorates the cycling performance and limits the energy density.

* Corresponding author.

** Corresponding author.

E-mail addresses: zhanghj18@hotmail.com (H. Zhang), yy2664@columbia.edu (Y. Yang).

¹ Z. Li, A. Li, and H. Zhang contributed equally to this paper.

Limited strategies by far have been explored to stabilize PEO-based electrolytes with 4 V cathodes. For example, $\text{Li}_{1.3}\text{Al}_{0.3}\text{Ti}_{1.7}(\text{PO}_4)_3$ (LATP) was demonstrated to protect LCO, which allowed $\text{Li}|\text{LCO}$ cells with PEO-based electrolyte charged up to 4.2 V, but the capacity retention was only 93% after 50 cycles, and low Coulombic efficiency (CE) less than 90% was observed in the entire 50 cycles, suggesting notable side reactions [30]. A poly (ethyl α -cyanoacrylate) coating was reported to improve the cycling performance when charged to 4.45 V. Nevertheless, the capacity only remained at about 75 mAh g^{-1} with poor retention of $\sim 43\%$ after 50 cycles [31]. Lithiated Nafion (Lithion) was recently reported to stabilize NCM 622 with diglyme-based electrolyte up to 4.2 V vs Li^+/Li [32], however, only 1 wt% of PEG-100kDa was dissolved in the liquid diglyme host, and the capacity retention is 85%/80 cycles with PEG-100kD addition.

To further improve the cycling stability and increase charging cut-off voltage, we demonstrate a strategy to take synergy of ceramic electrolyte coating and salt combination for stabilizing the 4 V cathode/PEO interface. A layer of LAGP ceramic electrolyte nanoparticle is first formed on LCO surface by scalable ball milling and sintering method. Then lithium bis-(oxalato)borate (LiBOB) is added as a salt, which is expected to decompose on cathode surface to form a surface coating, especially passivating pinholes in the LAGP layer, further reducing the oxidation of PEO. As the LAGP is only 3.5% compared to the mass of active cathode materials, energy density is not significantly sacrificed while it remarkably enhances cycling performance. By deploying the synergy of these two approaches, high capacity retentions of 81.9% over 400 cycles and 84.7% over 200 cycles are achieved in $\text{Li}|\text{PEO}|\text{LAGP-LCO}$ cells at 60 °C with charging cut-off of 4.25 V and 4.3 V, respectively. The stability is further validated in harsher conditions, wherein capacity retention of 88.1%/70 cycles when charged to 4.4 V, and 88.5%/150 cycles at room temperature (RT) are observed. This strategy can also be generalized to NCM, and steady cycling of 93.8% over 100 cycles is observed in $\text{Li}|\text{PEO}|\text{NCM523}$ cells. Moreover, these PEO-based electrolytes do not catch fire when ignited (Supporting video). This investigation provides an avenue in reinforcing interfacial stability between cathodes and electrolytes which is not stable with 4 V or higher operation voltage and improving their specific capacities and thermal stability.

Supplementary video related to this article can be found at <https://doi.org/10.1016/j.nanoen.2020.104655>

2. Experimental section

2.1. Synthesis of LAGP-coated LCO particles

LCO cathode material and LAGP powder were purchased from MTI Corporation and used as received. Firstly, LCO and LAGP nanoparticles were ball-milled together with a weight ratio of 96.5: 3.5, in which isopropanol was used as the milling medium. Then the composite was dried and sintered at 650 °C for 4 h with a ramping rate of 2.5 °C per minute. The obtained sample denoted as LAGP-LCO.

2.2. Preparation of electrolytes

The tri-salt electrolyte was prepared by mixing 0.3 M lithium bis(trifluoromethanesulfonyl) imide (LiTFSI) (Gotion Inc.), 0.2 M lithium bis(oxalato) borate (LiBOB) (Gotion Inc.) and 0.025 M LiPF_6 (Gotion Inc.) in poly(ethylene glycol) (PEO) (Sigma-Aldrich, average Mn ~ 10000)/poly(ethylene glycol) dimethyl ether (PEGDME) (Sigma-Aldrich, average $M_w \sim 500$), where PEO/PEGDME were mixed with 1: 1 by weight. In PEO-based electrolyte, 25 wt% ethylene carbonate (EC) (Sigma-Aldrich, 99%)/propylene carbonate (PC) (Sigma Aldrich, 99.7%) with volume ratio 3: 7 was used as plasticizer. Liquid electrolyte of 1.2 M LiPF_6 in EC/ethyl methyl carbonate (EMC) (EC: EMC = 3: 7, v/v) was kindly provided by Gotion Inc.

2.3. Material characterizations

Crystal structures of bare LCO and LAGP-LCO were collected by a PANalytical XPert3 Powder X-ray Diffraction (XRD) with Cu K α radiation. X-ray photoelectron spectroscopy (XPS) spectra of LAGP-LCO powder and cycled electrode were recorded on Phi 5500 XPS with Al X-ray source applied. Flow etching was used to get the information under different depths of LAGP-LCO cathode after cycling. Morphology of samples was characterized on SIGMA VP Zeiss scanning electron microscopy. Before XPS and scanning electron microscope (SEM) testing, the cycled LAGP-LCO cathode and Li metal samples were washed with pure PC to eliminate electrolyte residue, and then fully dried under vacuum. To avoid contamination, the samples were transferred from glovebox to XPS and SEM instruments in a sealed container filled with Ar gas. The PEO oxidation products were determined by ^1H nuclear magnetic resonance (NMR) in pure deuterated Dimethyl sulfoxide-D6 using a Bruker Advance III (300 MHz) spectrometer at room temperature. The detailed morphology of LAGP-LCO particle and electrode after cycling were conducted with an FEI TALOS F200X transmission electron microscopy. The LAGP-LCO particle for transmission electron microscopy (TEM) analysis was prepared by drop-casting a LAGP-LCO ethanol dispersion onto a lacy carbon TEM grid. For TEM analysis of cathode after cycling, the samples were sectioned by an FEI Helios NanoLab 660 SEM/FIB system. The TEM specimens were thinned by a 30 kV Ga ion beam and further cleaned with the aid of a 5 kV Ga beam.

2.4. Synchrotron techniques

The LCO and LAGP-LCO cathodes after cycling were studied by X-ray absorption near edge spectroscopy (XANES) at FXI (18-ID), and soft X-ray absorption (XAS) at IOS (23-ID-2) beamline at the National Synchrotron Light Source II. At FXI (18-ID), the full-field two-dimensional (2D) XANES with 30 nm spatial resolution across Co K-edge was conducted with transmission X-ray microscopy (TXM). The XANES spectrum at each pixel was fitted with the standard LCO at 3 V and LCO charged at 4.3 V with carbonate liquid electrolyte as reference standards. XAS spectra were acquired using a Vortex EM silicon drift detector. O K-edge and Ge L-edge were collected in partial fluorescence yield (PFY) mode, while Co L-edge was measured in the inverse partial fluorescence yield (IPFY) mode by monitoring the non-resonant O fluorescence in order to reduce distortions from self-absorption effects.

2.5. Battery assembly

LAGP-LCO or bare LCO cathode was prepared by mixing LAGP-LCO or LCO powder, SUPER C65 conductive carbon (Timcal) and poly(vinylidene fluoride) (Kynar 761, Arkema) with a mass ratio of 85: 8: 7 in N-methyl-2-pyrrolidone (99%, Sigma Aldrich) to form a homogeneous slurry. Then the slurry was coated on an aluminum foil and dried overnight at 110 °C, followed by an assembly in CR2032 coin-type cells. The batteries were constructed using bare LCO or LAGP-LCO electrode (active material $\sim 6.2 \text{ mg cm}^{-2}$ or $\sim 10.5 \text{ mg cm}^{-2}$), lithium metal anode chip (250 μm or 40 μm thick, 1.56 cm diameter), one-piece monolayer polypropylene separators (Celgard 3501, 25 μm) and PEO-based electrolytes. Before cell assembly, PEO electrolyte was infiltrated into the cathode. All of the cells, including $\text{Li}|\text{Li}$ symmetric cells, $\text{Li}|\text{LAGP-LCO}$ cells, and $\text{Li}|\text{LCO}$ cells, were assembled in an argon-filled glove box with moisture and oxygen levels below 0.1 and 0.1 ppm, respectively.

2.6. Electrochemical measurements

Electrochemical impedance spectroscopy (EIS) was tested on a VMP3 multichannel potentiostat from Bio-Logic in a frequency range of 1 MHz to 0.1 Hz with a 10 mV amplitude. Cyclic voltammetry (CV) of $\text{Li}|\text{LCO}$ and $\text{Li}|\text{LAGP-LCO}$ cells were also executed on Bio-Logic from 3 V to 4.4 V

with a scanning speed of 0.1 mV/s. Both galvanostatic cycling of Li|Li symmetric cells, Li|LCO and Li|LAGP-LCO cells were conducted on battery tester (Wuhan LAND Electronics Co. Ltd.). Cycling performance and rate capability of Li|LCO and Li|LAGP-LCO cells were carried out with constant current and constant voltage mode using battery testers. When the cells reached the charge cut-off voltage, a constant voltage charge process was applied until the current decreased to 0.05 C. The EIS, CV and rate performance were conducted at 60 °C. The cycling performance was tested at 60 °C, 40 °C or RT.

3. Results and discussion

LAGP is chosen as the coating material since it has reasonably high ionic conductivity ($2 \times 10^{-3} \text{ S cm}^{-1}$) [33], and excellent chemical stability with 4 V cathodes [34]. Nano-LAGP coating was formed by a simple and scalable ball milling and sintering method. LCO and LAGP nanoparticles were ball-milled in isopropanol with a ratio of 96.5: 3.5 by weight. The mixture was then dried and sintered at 650 °C to form better bonding between LAGP and LCO. Since the ceramic coating still has grain boundaries and pinholes, which could induce PEO oxidation, we carefully choose salt content so that a passivating layer can be formed on LAGP-LCO surface from *in-situ* decomposition during cycling (Fig. 1a). The synergy of these two approaches allows facile transportation of Li^+ but forms an energy barrier to resist the oxidation of PEO electrolytes (Fig. 1b and c). Moreover, imperfections in the LAGP coating allows for electronic contact between carbon black and LCO before the *in-situ* decomposition of electrolyte, and such limited imperfections are further passivated by the *in-situ* decomposition process so that the cycling reversibility is not deteriorated.

The as-prepared LAGP-LCO samples show the same XRD pattern as pristine LCO (Fig. S1, JCPDS No. 75–0532). The existence of LAGP on LCO surface is confirmed by XPS, showing the Ge peak at 32.6 eV for Ge^{4+} (Fig. S2). SEM images show that LCO particles with smooth surface become rough and are decorated with LAGP nanoparticles (Fig. 2a and Fig. S3). Energy dispersive spectrometry (EDS) mapping of a single LAGP-LCO particle (Fig. 2b) shows clear signals from Co and Ge. The noise in Ge mapping is due to the weak signal of Ge as its percentage is low, but Ge signal is indeed richer on the particle. TEM analysis further illustrates a ~20–50 nm LAGP coating on LCO together with scattered LAGP nanoparticles (Fig. 2c), suggesting that LAGP permeates LCO well and spread on LCO surface during the sintering process. Diffraction pattern (DP) of region 1 clearly shows rings matching with (110) and

(211) planes of LAGP (Fig. 2d, JCPDS No. 80–1924). The DP of region 2 corresponds to layer LCO (R-3m space group) together with dim rings matching LAGP (Fig. 2e). The LAGP nano-coating is further confirmed by EDS mapping, where Ge, Al and P signals spread over the LCO particle (Fig. 2f, Fig. S4). All these results demonstrate that LAGP nanoparticles are successfully coated on LCO but they do not change the crystal structure of bulk LCO.

The electrolyte is composed of 0.3 M LiTFSI, 0.2 M LiBOB and 0.025 M LiPF₆ in PEO/PEGDME (PEO: PEGDME = 1: 1, by weight), where PEGDME is short for polyethylene glycol dimethyl ether ($M_w = 500$) and the PEO has an M_w of 10,000. The reason for choosing this salt combination is that LiTFSI helps enhance ionic conductivity, and LiBOB and LiPF₆ can decompose over 4 V and passivate the cathode surface and helps avoid Al corrosion during cycling [10,35]. The as-prepared electrolyte shows ionic conductivities of $7.8 \times 10^{-6} \text{ S cm}^{-1}$ at RT, which increases to $7.0 \times 10^{-4} \text{ S cm}^{-1}$ at 60 °C (Fig. 2g). The conductivity can be further enhanced to $2.3 \times 10^{-4} \text{ S cm}^{-1}$ at RT and $1.1 \times 10^{-3} \text{ S cm}^{-1}$ at 60 °C by adding 40 wt% Ta-doped $\text{Li}_7\text{La}_3\text{Zr}_2\text{O}_{12}$ (LLZO) solid electrolyte particles. The PEO electrolytes are solid at RT (Fig. 2h). They are also fire-retardant and show excellent thermal stability, as characterized by resistance to ignition (Fig. 2i and Supporting video). The electrolytes also show steady cycling in Li|Li symmetric cells. At 0.3 mA cm⁻² and 0.3 mAh cm⁻², the overpotential of Li|Li cells only increases from 80 to 120 mV over 2000 h (Fig. S5). The overpotential of the Li|Li cell slightly increases from 240 mV to 400 mV over 880 h at 0.3 mA cm⁻² and 1 mAh cm⁻² (Fig. S6). The surface of Li metal maintains pretty densely after cycling (Fig. S7 and Fig. S8), suggesting good interfacial stability between the electrolyte and Li metal.

To evaluate the performance of the proposed strategy, Li|LAGP-LCO cells were tested in the range of 3–4.25/4.3/4.4 V at 60 °C. The current rate is 0.3 C for charging with a constant voltage step down to 0.05 C and 0.5 C for discharge (1 C = 145 mA g⁻¹), after one cycle at 0.1 C. First, in the range of 3–4.25 V, the Li|LAGP-LCO cell shows excellent cycling performance with 131.2 mAh g⁻¹ in the first cycle and 107.4 mAh g⁻¹ after 400 cycles, which represents a capacity retention of 81.9% (Fig. 3a and b), or only 0.05% decay per cycle. Moreover, the CE is 87.3% for the first cycle and then reaches averagely 99.9% for the following cycles, indicating nearly no side reaction due to PEO oxidation. In contrast, the Li|LCO cell shows a steady capacity drop from 135.1 mAh g⁻¹ to only 22.2 mAh g⁻¹ after 100 cycles (Fig. 3a and c). Its CE also fluctuates between 95 and 99% and averages at 97.8% for the first 100 cycles. These results demonstrate that the LAGP nano-coating is necessary for

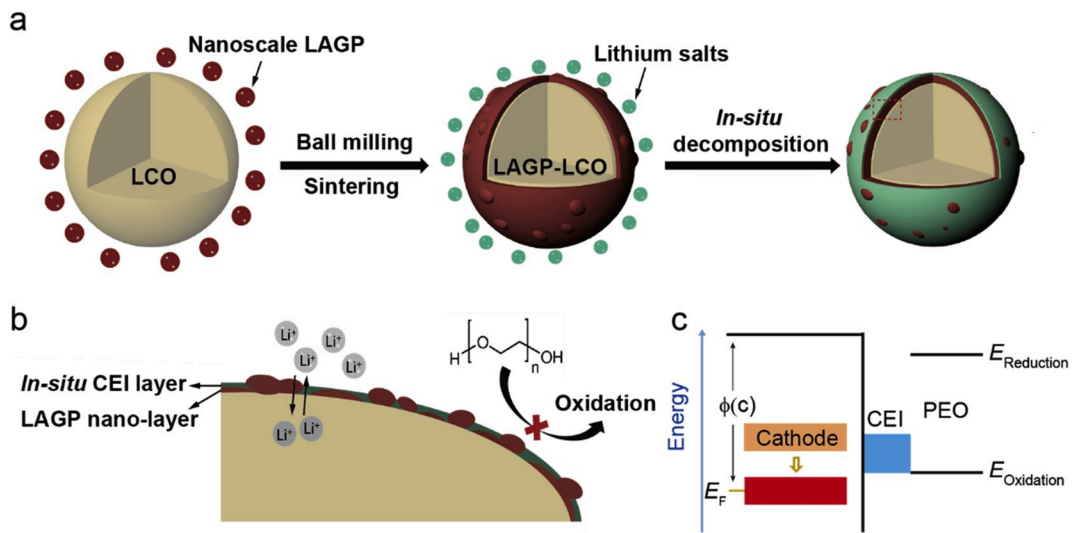
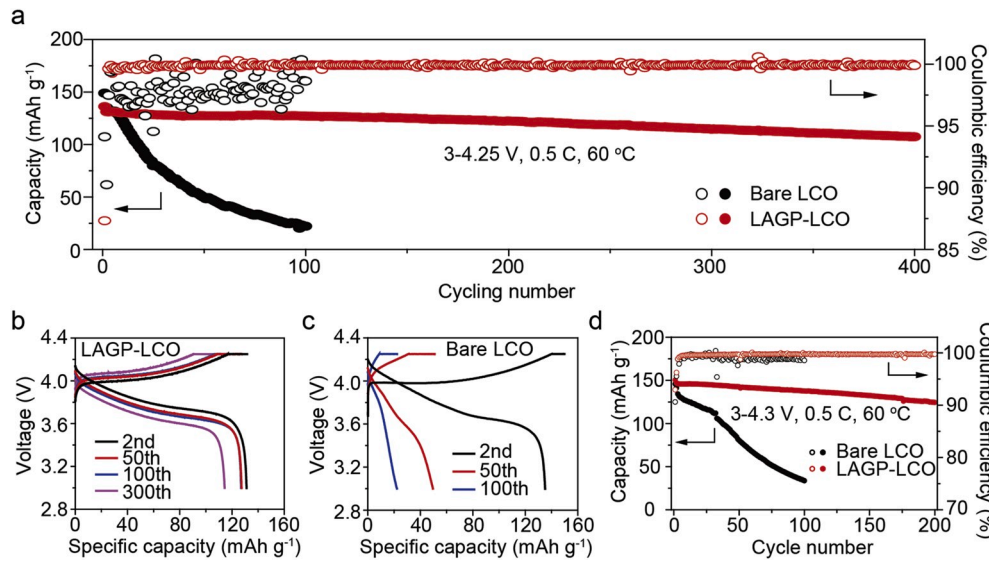
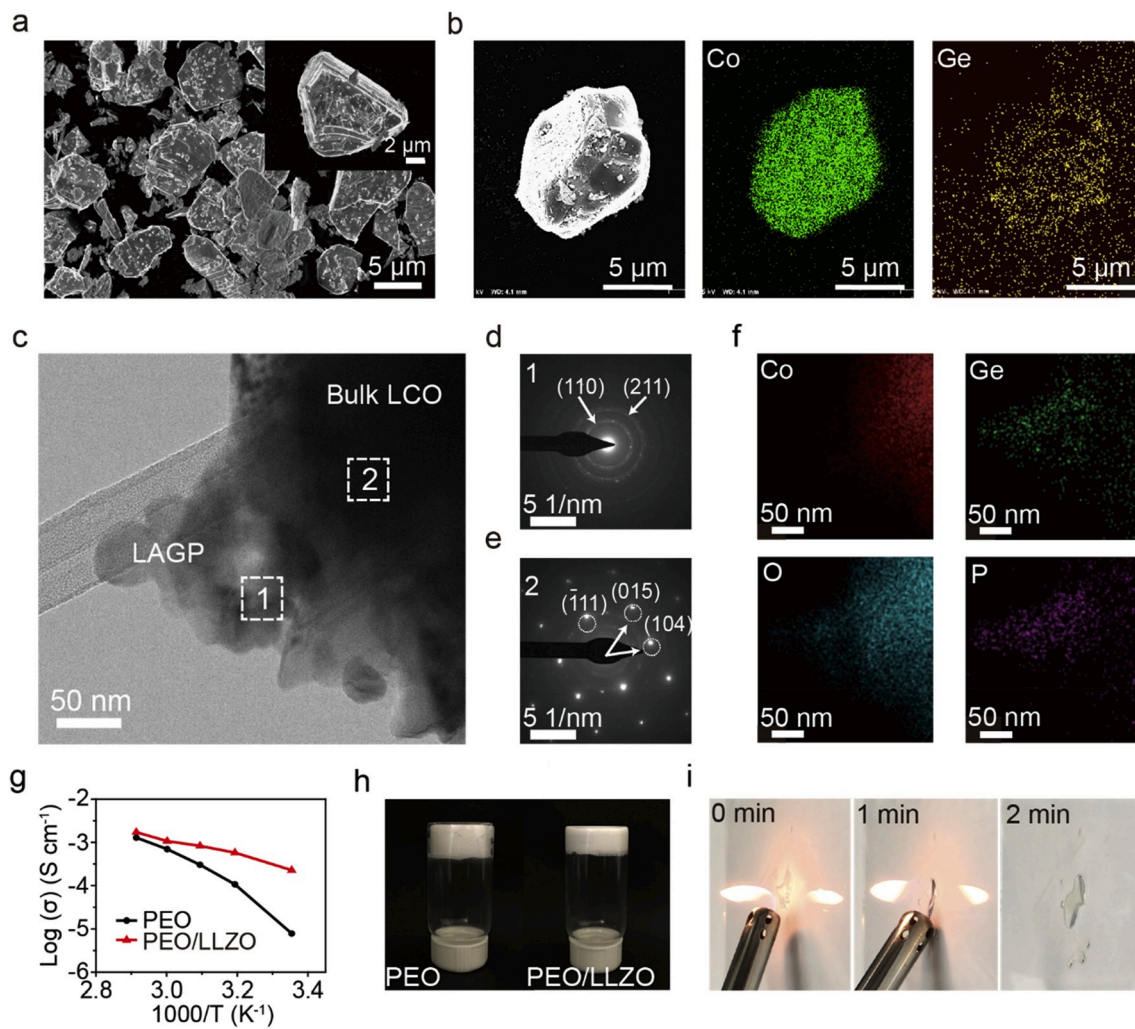


Fig. 1. The schematic illustration for (a) the synthetic process to produce both LAGP nano-coating and salt-based passivation. (b) The schematic of the two strategies on cathode surface. (c) Proposed mechanism to form energy barrier to suppress PEO oxidation and stabilize the interface between LCO and PEO-based electrolytes. The two layers are from LAGP nano-coating and products from *in-situ* salts decomposition, respectively.



suppressing side reactions and stabilizing the LCO/electrolyte interphase.

Significantly enhanced stability is also observed when the cut-off voltage increases to 4.3 V and 4.4 V. At 4.3 V, Li|LAGP-LCO cell shows an initial specific capacity of 150.4 mAh g^{-1} at 0.1 C and 147.0 mAh g^{-1} at 0.5 C, and slightly decreases to 132.4 mAh g^{-1} over 200 cycles with a capacity retention of 84.7% (Fig. 3d and Fig. S9a). In contrast, Li|LCO cell shows rapid decay from 141.4 to 33.8 mAh g^{-1} after 100 cycles (Fig. 3d and Fig. S9b). The CE for Li|LAGP-LCO cell is ~99.7% in most cycles, while for bare LCO, CE decreases below 98.8% after 30 cycles, indicating strong side reactions. Then we increase the areal capacity to 1.58 mAh cm^{-2} . The Li|LAGP-LCO cell shows initial capacity as 150.4 mAh g^{-1} at 0.5 C with a retention of 89% after 80 cycles, while the capacity of Li|LCO cell decays fast from 131.2 mAh g^{-1} to 51.9 mAh g^{-1} in 50 cycles (Fig. 4a).

When further charged to 4.4 V, the initial specific capacity reaches 169.2 mAh g^{-1} at 0.1 C and 163.7 mAh g^{-1} at 0.5 C for LAGP-LCO, which drops to 162.5 mAh g^{-1} after 20 cycles, and 141.2 mAh g^{-1} after 70 cycles, representing capacity retention of 86.3% (Fig. S10a). The corresponding average CE is 99.4%. The overpotential slightly increases from 0.05 V to 0.1 V after 20 cycles and 0.2 V after 70 cycles (Fig. S10b). In contrast, the specific capacity of bare LCO decreases from 165.0 to 37.2 mAh g^{-1} after only 20 cycles (Fig. S10a) and the overpotential increases from 0.04 to 0.7 V (Fig. S10c). The average CE is only 94.1%. The improved cycling performance is also confirmed by cyclic voltammetry (CV) (Fig. S11). These data with 4.3 and 4.4 V cut-off demonstrate the effectiveness of the proposed strategy for enabling stable LCO/PEO interface.

Besides LAGP nano-coating, the salt combination is also important. When Li|LAGP-LCO cell is combined with LiBF₄/PEO, the capacity decays fast (10.8% retention/100 cycles) with a low average CE of 96.9% (Fig. S12a). The Li|LAGP-LCO cell utilizing LiPF₆/PEO electrolyte cannot be fully charged after two cycles (Fig. S12b). Moreover, the Li|LAGP-LCO cell with LiPF₆-free electrolyte shows a noticeably faster drop of capacity (Fig. S12c), which may be due to the corrosion of

aluminum current collector and worse cycling of lithium anode [35]. Additionally, concentrated 1 M LiTFSI + 1 M lithium difluoro(oxalate) borate (LiDFOB) in PEO/PEGDME also fail to enable stable cycling in Li|LCO cell (Fig. S12d) as its 1,2-dimethoxyethane counterpart [10]. These results suggest that solely LAGP is not enough to prevent PEO oxidation and the passivation layer from salt decomposition is also critical for stable cycling. The suppressed Al corrosion in the LiTFSI/LiBOB/LiPF₆ system is verified by CV test and SEM. Among three electrolyte systems, the one with LiTFSI/LiBOB/LiPF₆ salt shows the lowest oxidation current in the CV test and the smoothest surface of Al foil after the test, indicating the smallest degree of Al corrosion (Fig. S13 and Fig. S14). Hence, the results prove the importance of LAGP nano-coating, as well as the combination of LiTFSI/LiBOB/LiPF₆ salts, which synergize to produce stable cycling in PEO-based electrolyte with LCO cathode.

In addition to providing cycling stability, the LAGP-LCO also provides good power capability at 60 °C, featuring a reversible specific capacity of 140.6, 138.5, 134.6, and 118.3 mAh g^{-1} at 0.1 C, 0.3 C, and 0.5 C, and 1 C in 3–4.25 V, respectively. In contrast, bare LCO cell shows the specific capacity of 143.1, 136.7, 128.4, and 95.7 mAh g^{-1} at 0.1 C, 0.3 C, 0.5 C, and 1 C, respectively (Fig. S15), lower than that of LAGP-LCO at high rates.

In order to comprehensively evaluate the performance of the proposed strategy in 4 V cathode, we further test their performance at various conditions, such as cycling at RT, combining with thin Li anode ($40 \mu\text{m}$), replacing LCO with NCM523, and the addition of LLZO ceramic electrolyte particles. Steady cycling has been observed in all cases, as discussed below.

First, although 60 °C can be an acceptable temperature for electric vehicles, it is ideal to have battery functional at RT. With the addition of 25 wt% EC/PC plasticizer inside, the ionic conductivity of PEO electrolyte reaches $5.1 \times 10^{-4} \text{ S cm}^{-1}$ at RT (Fig. S16a). Consequently, capacity retention of 88.5% over 150 cycles is achieved at 0.2 C at RT (Fig. 4b). The coulombic efficiency of this Li|LAGP-LCO cell fluctuates between 98.8% and 101.7%, which is mainly due to the variation of room temperature. Similarly, the retention of 93.0%/200 cycles is

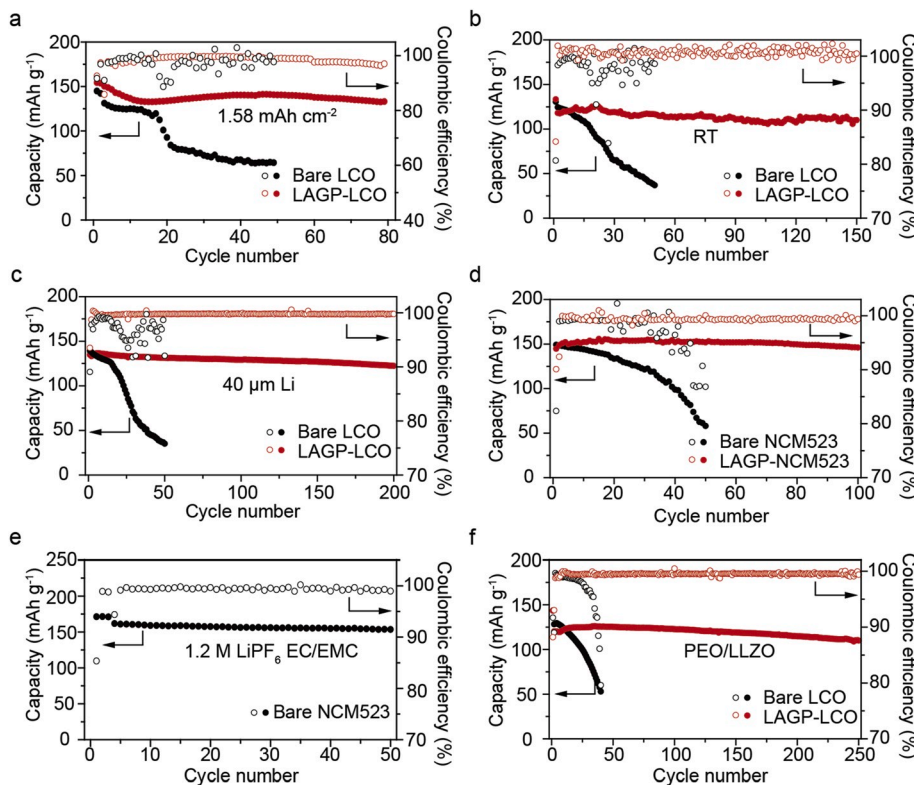


Fig. 4. Cycling performance (solid dots) and CE (open dots) of Li|4 V cathode cells at various conditions. (a) Li|LCO and Li|LAGP-LCO cells with an areal capacity of 1.58 mAh cm^{-2} at 0.5 C in 3.0–4.3 V. (b) Li|LCO and Li|LAGP-LCO cells at RT and 0.2 C in 2.7–4.3 V. The electrolyte is 0.6 M LiTFSI + 0.4 M LiBOB + 0.05 M LiPF₆ in PEO/PEGDME/EC/PC (PEO: PEGDME: EC/PC = 2: 1, by weight). (c) Li|LCO and Li|LAGP-LCO cells with PEO electrolyte and $40 \mu\text{m}$ Li at 0.3 C in 3.0–4.25 V. (d) Li|NCM523 and Li|LAGP-NCM523 cells with PEO-based electrolyte at 0.3 C in 3.0–4.3 V. (e) Li|NCM523 and cells with liquid electrolyte of 1.2 M LiPF₆ EC/EMC at 0.3 C in 3.0–4.3 V. (f) Li|LCO and Li|LAGP-LCO cells with PEO/LLZO-based electrolyte at 0.5 C discharge in 3.0–4.25 V. All cells were pre-cycled at 0.1 C and cells in (a), (c), (d), (e), (f) were tested at 60 °C.

observed at 40 °C (Fig. S16b). When further increasing the ratio of EC/PC to 50 wt%, the cells can discharge at 1 C at RT (Fig. S17). Besides RT operation, we also test cells with 40 μm-thin lithium instead of conventional 250 μm-thick lithium. Capacity retention of 89.7% is reached after 200 cycles for 3–4.3 V at 60 °C (Fig. 4c). Although the cathode loading is only ~1 mAh cm⁻², this still indicates that the CE is at least 96%, much higher than ~90% in conventional carbonate electrolyte [25,36,37]. These results support that PEO is an attractive electrolyte for lithium metal batteries, but more tests are needed to evaluate the exact performance of PEO with Li metal.

While LCO is a model 4 V cathode, NCM is the standard material in electric vehicles. Thus, the proposed strategy is further tested in NCM523. As shown in Fig. 4d, LAGP-coated NCM523 shows capacity retention of 93.8%/100 cycles for 3–4.3 V at 60 °C, much better than bare NCM523 (39.2%/50 cycles). Meanwhile, the bare NCM523 with commercial electrolyte of 1.2 M LiPF₆ EC/EMC shows steady cycling with capacity retention of 95%/50 cycles (Fig. 4e), validating that NCM523 itself is stable and its quality is not the reason for capacity fading with PEO electrolyte. On the other side, the strategy can also be extended to polymer/ceramic composite electrolytes. With 60 wt% of PEO/LLZO or 80 wt% of PEO/PEGDME/LLZO, steady performance of 87.2% over 250 cycles is observed for 3–4.25 V at 60 °C (Fig. 4f). When LLZO is replaced by Al₂O₃, stable cycling performance is also achieved (Fig. S18). These cycling data are summarized as Table 1 below and they no doubt prove the effectiveness and generalizability of the proposed strategy. However, it should be noted that the RT tests is just to show cycling stability at RT, but the mass loading is much smaller than required for practical batteries. It also should be noted that NCM with higher Ni content should also be tested to evaluate compatibility with Ni-rich oxides.

To better understand how the proposed strategy on interfacial engineering stabilizes the LCO/PEO interface and lead to steady cycling, multi-modal characterizations are carried out including NMR, TEM, EIS, TXM with XANES [38], and XAS.

First, the PEO oxidation product is analyzed by the ¹H NMR spectroscopy. PEO electrolyte after 300 cycles with bare LCO shows a new peak at the chemical shift of 9.72 ppm (Fig. S19), which is identified as a proton in the aldehyde group due to oxidation [39]. In contrast, such peak is observed in neither pristine PEO electrolyte nor that after 300 cycles with LAGP-LCO, demonstrating that the PEO oxidation is effectively suppressed with the nanoscale protection from the ceramic electrolyte and the salt decomposition.

To further validate that the nanoscale coating suppresses the oxidation rate of PEO, leakage current density (*j*_{leak}) tests are then carried out. LCO cathodes are charged to 4.25 V vs Li⁺/Li at 0.1 C and 60 °C followed by holding at 4.25 V. The bare LCO/PEO cell shows a gradually reduced tail and the steady-state *j*_{leak} is 0.37 mA g⁻¹ LCO, indicating severe oxidation. In contrast, the current of LAGP-LCO/PEO drops rapidly during holding, and *j*_{leak} is only 0.19 mA g⁻¹ LCO, close to bare LCO in conventional EC/DEC electrolytes (0.14 mA g⁻¹ LCO, Fig. 5a). This means that once the interfacial coating is formed, the magnitude of side reaction is reduced to as low as commercial carbonate electrolytes. The reduced oxidation also leads to much more stable impedance in EIS. With LAGP coating, the impedance only slightly changes from 129.7 to

138.7 Ω at 0.1 Hz after 100 cycles (Fig. 5b). In contrast, significantly increased impedance from 323.7 to 706.3 Ω is observed in Li|LCO cells after cycling (Fig. 5c). A closer look illustrates that the PEO oxidation has little effect on the resistance of bulk electrolyte (24.7 Ω in the 1st cycle vs. 21.0 Ω in the 100th cycle), and charge transfer resistance (210.3 Ω in the 1st cycle vs. 160.1 Ω in the 100th cycle) in the bare LCO sample. However, it leads to significantly longer diffusion tail at low frequency, which is typically signed to ion diffusion in the solid phase.

To understand why PEO oxidation affects ion diffusion in the solid phase, high-resolution TEM is used to image LCO particles after 50 cycles. As shown in Fig. 5d, the bare LCO surface becomes less crystalline and even partially amorphous. Obvious directional change of crystal planes is also observed. The corresponding DP shows diffusive spots, indicating poor crystallinity and more defects (Fig. 5d, inset). This is further confirmed by cycling dead bare LCO cell with fresh Li and carbonate liquid electrolyte, where the capacity cannot be fully recovered (Fig. S20). On the other side, in LAGP-coated protected LCO, LAGP coating still remains after 50 cycles (Fig. S21). The TEM image shows that an amorphous layer is formed on LCO surface after cycling, which is considered to arise from salt decomposition from the electrolyte (Fig. 5f). The passivation layer from salt decomposition can also be inferred from XPS. LiF (~685 eV) and Li_xPO_yF_z (~686.5 eV) in F1s are found in the cycled cathode (Fig. S22), which may come from the decomposition of LiTFSI and LiPF₆. Hence, with such protection, the LCO still has clear layered structure near-surface and shows sharp points in DP, even for the region not obviously covered by LAGP (Fig. 5e). These results indicate that PEO oxidation causes damage to LCO particles (e.g. electrolyte/cathode reaction at high electrode potential), reduce its crystallinity and thus slow down ion diffusion inside. The effect of salt on cathode electrolyte interphase (CEI) composition will be further studied in the future.

One potential question in this explanation is why the interfacial damage leads to an elongated diffusion tail in EIS, instead of charge transfer resistance. The answer to this is that the slow ion diffusion in damaged region and time scale in EIS (10 s for 0.1 Hz) means that ions only diffuse in the order of ~10 nm (Supporting note). This is qualitatively validated by COMSOL simulation (Fig. S23). Even a 5 nm-thick surface layer with low diffusivity of ~10⁻¹⁵ cm² s⁻¹ can produce a similar diffusion tail. In contrast, pristine LCO surface with high diffusivity (10⁻¹¹ cm² s⁻¹) leads to negligible diffusion tail, which aligns well with Fig. 5b and c. The detailed degradation mechanisms will be further investigated in the future.

The sluggish ion diffusion makes it difficult for Li⁺ to insert into bare LCO and blocks Co⁴⁺ reduction, which is consistent with observations in XANES, XAS, and XRD. In Co XANES spectra at ~7.73 keV (Fig. 5g), LAGP-coated LCO after 50 cycles and discharged to 3.0 V shows the correct oxidation state (7.727 keV corresponding to Co³⁺, Fig. S24 as the reference). Comparatively, the spectra of cycled bare LCO at 3.0 V shifts to 7.729 keV, corresponding to oxidation state similar to that at 4.3 V (Li_{0.5}CoO₂, Fig. S24), suggesting that Li⁺ cannot intercalate inside to reduce Co⁴⁺. Results in such ensemble-averaged spectra are further confirmed by spatially resolved 2D TXM XANES images, showing that LAGP-LCO remains in 3 V state (Fig. 5h), while most regions in bare LCO remain at the 4.3 V state even when discharged to 3.0 V (Fig. 5i). Such

Table 1

Summary of capacity retention and CE in Li|LCO and Li|LAGP-LCO cells at different conditions.

Testing condition	4.25 V, 60 °C		4.3 V, 60 °C		4.4 V, 60 °C	
Cathode	LAGP-LCO	Bare LCO	LAGP-LCO	Bare LCO	LAGP-LCO	Bare LCO
Capacity retention (/cycle number)	81.9%/400	16.4%/100	84.7%/200	23.9%/100	86.3%/70	22.5%/20
Average CE	99.9%	97.8%	99.7%	98.8%	99.4%	94.0%
Testing condition	4.3 V, RT		4.3 V, 60 °C, 40 μm Li		4.3 V, 60 °C, NCM523	
Cathode	LAGP-LCO	Bare LCO	LAGP-LCO	Bare LCO	LAGP-NCM	Bare NCM
Capacity retention (/cycle number)	88.5%/150	29.7%/50	89.7%/200	25.5%/50	93.8%/100	39.2%/50
Average CE	98.8–101.7%	97.6%	99.7%	96.6%	99.3%	96.6%

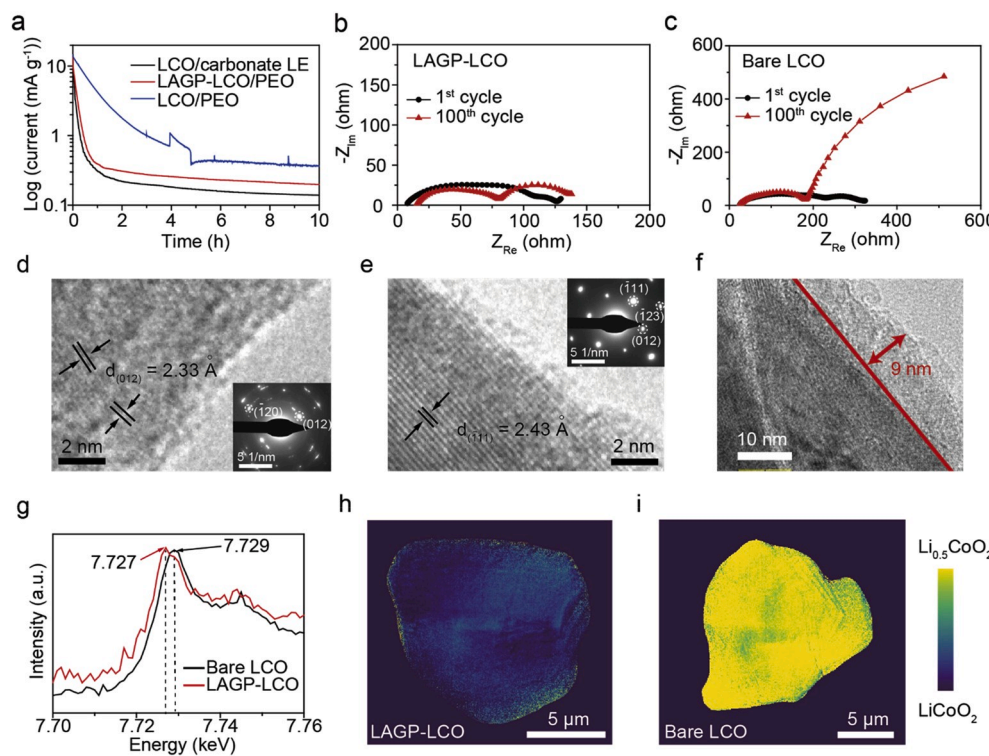


Fig. 5. Characterizations of cycled bare LCO and LAGP-LCO cathode. (a) Leakage current of Li|LAGP-LCO and Li|LCO cells with PEO-based electrolyte and Li|LCO cell with carbonate liquid electrolyte (1 M LiPF₆ in EC/EMC) at 60 °C. (b, c) EIS results of (b) Li|LAGP-LCO and (c) Li|LCO cells between 1 MHz and 0.1 Hz. All data were taken at the charged state (4.25 V). (d, e) High-resolution TEM images of (d) bare LCO and (e) LAGP-LCO cycled electrodes. The inset images are corresponding diffraction patterns. (f) A TEM image of a LAGP-LCO particle at the charged state (4.3 V) after 300 cycles. The salt decomposition layer can be observed. (g) The Co K-edge spectra of LCO and LAGP-LCO particle at the discharge state (3 V). (h, i) Representative 2D XANES chemical maps of Co on (h) a LAGP-LCO particle and (i) a bare LCO particle after 50 cycles. Both electrodes were imaged at the discharge state (3 V).

results are also consistent with O K-edge and Co L-edge observed in soft XAS spectra (Fig. S25 and Fig. S26), in which O K-edge of bare LCO at 3 V shows a strong shoulder at 528.5 eV and Co L-edge at 3 V shifts toward the higher energy region by ~0.4 eV. These indicate that the bare LCO remains in Co⁴⁺-rich state instead of being reduced to Co³⁺ [40,41]. In addition, XRD shows that the (003) peak in bare LCO discharged to 3.0 V after 50 cycles remains in the charged state (4.3 V, 18.54° in 2θ), while this peak in LAGP-coated LCO shifts to that for pristine LCO at 18.93° in 2θ (Fig. S27).

Based on these multi-modal characterization data above, it can be concluded the underlying mechanism behind sluggish ion diffusion is that the active surface of LCO results in fast PEO oxidation, which induces defects and damages crystallinity of the solid cathode as well. The proposed interfacial engineering strategy can successfully suppress the PEO oxidation and maintain the high crystallinity of LCO to ensure facile ion transport inside, which is the key to the stable cycling and success of this strategy.

4. Conclusions

In summary, we have demonstrated that a nanoscale interfacial engineering strategy can enhance the stability between 4 V LCO electrode and PEO-based electrolyte. The synergy of a LAGP ceramic electrolyte coating and a passivation layer from salt decomposition together protects PEO from oxidation over 4 V. Excellent cycling performance of 81.9% over 400 cycles is achieved in the voltage range of 3–4.25 V at 60 °C. When charged to a higher voltage, the Li|LAGP-LCO cell show stable cycling with capacity retentions of 90.1%/150 cycles, 88.1%/70 cycles for 4.3 and 4.4 V, respectively. Stable cycling at RT and with NCM523 is also successfully achieved. The reversible cycling even at 60 °C suggests that the interface is highly stable at elevated temperature, where interfacial instability is typically accelerated. These results open new approaches to stabilize the electrode/electrolyte interface and develop lithium metal batteries with high energy density.

Declaration of competing interest

This work described has not been published previously (except in the form of an abstract, a published lecture or academic thesis), that it is not under consideration for publication elsewhere, that its publication is approved by all authors and tacitly or explicitly by the responsible authorities where the work was carried out, and that, if accepted, it will not be published elsewhere in the same form, in English or in any other language, including electronically without the written consent of the copyright-holder.

Acknowledgements

A. J. Li would like to acknowledge the financial support from the China Scholarship Council (No. 201706010086) and X. Y. Chuan acknowledges the National Natural Science Foundation of China (No. 51774016). This research used resources of the Center for Functional Nanomaterials, which is a U.S. DOE Office of Science Facility, and the Scientific Data and Computing Center, a component of the Computational Science Initiative, at Brookhaven National Laboratory under Contract No. DE-SC0012704. Dr. R. Q. Lin and Dr. X.-Q. Yang were supported by the Assistant Secretary for Energy Efficiency and Renewable Energy, Vehicle Technology Office of the U.S. Department of Energy (DOE) through the Advanced Battery Materials Research (BMR) Program, including Battery500 Consortium under contract DE-SC0012704. This research also used resources of the 23-ID-2 (IOS) and 18-ID (FXI) beamlines of the National Synchrotron Light Source II, a U.S. DOE Office of Science User Facility operated for the DOE Office of Science by Brookhaven National Laboratory under Contract No. DE-SC0012704. We also acknowledge Celgard LLC for providing polypropylene (Celgard 3501) separators.

Appendix A. Supplementary data

Supplementary data to this article can be found online at <https://doi.org/10.1016/j.nanoen.2020.104655>.

References

- [1] N.-W. Li, Y.-X. Yin, C.-P. Yang, Y.-G. Guo, *Adv. Mater.* 28 (2016) 1853–1858.
- [2] B. Liu, J.-G. Zhang, W. Xu, *Joule* 2 (2018) 833–845.
- [3] M. Armand, J.M. Tarascon, *Nature* 451 (2008) 652–657.
- [4] D. Larcher, J.M. Tarascon, *Nat. Chem.* 7 (2015) 19–29.
- [5] J. Qian, L. Liu, J. Yang, S. Li, X. Wang, H.L. Zhuang, Y. Lu, *Nat. Commun.* 9 (2018) 4918.
- [6] P. Albertus, S. Babinec, S. Litzelman, A. Newman, *Nat. Energy* 3 (2018) 16–21.
- [7] Y. Lu, Z. Tu, L.A. Archer, *Nat. Mater.* 13 (2014) 961–969.
- [8] B. Dunn, H. Kamath, J.-M. Tarascon, *Science* 334 (2011) 928.
- [9] J. Li, C. Ma, M. Chi, C. Liang, N.J. Dudney, *Adv. Energy Mater.* 5 (2015) 1401408.
- [10] S. Jiao, X. Ren, R. Cao, M.H. Engelhard, Y. Liu, D. Hu, D. Mei, J. Zheng, W. Zhao, Q. Li, N. Liu, B.D. Adams, C. Ma, J. Liu, J.-G. Zhang, W. Xu, *Nat. Energy* 3 (2018) 739–746.
- [11] X.-B. Cheng, R. Zhang, C.-Z. Zhao, Q. Zhang, *Chem. Rev.* 117 (2017) 10403–10473.
- [12] D. Andre, S.-J. Kim, P. Lamp, S.F. Lux, F. Maglia, O. Paschos, B. Stiaszny, *J. Mater. Chem. A* 3 (2015) 6709–6732.
- [13] A. Manthiram, X. Yu, S. Wang, *Nat. Rev. Mater.* 2 (2017) 16103.
- [14] D. Lin, Y. Liu, Y. Cui, *Nat. Nanotechnol.* 12 (2017) 194–206.
- [15] T. Jin, Y. Wang, Z. Hui, B. Qie, A. Li, D. Paley, B. Xu, X. Wang, A. Chitru, H. Zhai, T. Gong, Y. Yang, *ACS Appl. Mater. Interfaces* 11 (2019) 17333–17340.
- [16] H. Zhai, T. Gong, B. Xu, Q. Cheng, D. Paley, B. Qie, T. Jin, Z. Fu, L. Tan, Y.-H. Lin, C.-W. Nan, Y. Yang, *ACS Appl. Mater. Interfaces* 11 (2019) 28774–28780.
- [17] D.H.C. Wong, J.L. Thelen, Y. Fu, D. Devaux, A.A. Pandya, V.S. Battaglia, N. P. Balsara, J.M. DeSimone, *Proc. Natl. Acad. Sci. Unit. States Am.* 111 (2014) 3327.
- [18] Y. Kato, K. Hasumi, S. Yokoyama, T. Yabe, H. Ikuta, Y. Uchimoto, M. Wakihara, *Solid State Ionics* 150 (2002) 355–361.
- [19] S. Hess, M. Wohlfahrt-Mehrens, M. Wachtler, *J. Electrochem. Soc.* 162 (2015) A3084–A3097.
- [20] Z. Xue, D. He, X. Xie, *J. Mater. Chem. A* 3 (2015) 19218–19253.
- [21] X. Wang, H. Zhai, B. Qie, Q. Cheng, A. Li, J. Borovilas, B. Xu, C. Shi, T. Jin, X. Liao, Y. Li, X. He, S. Du, Y. Fu, M. Dontigny, K. Zaghib, Y. Yang, *Nano Energy* 60 (2019) 205–212.
- [22] X. Wang, Y. Zhang, X. Zhang, T. Liu, Y.-H. Lin, L. Li, Y. Shen, C.-W. Nan, *ACS Appl. Mater. Interfaces* 10 (2018) 24791–24798.
- [23] K. Fu, Y. Gong, J. Dai, A. Gong, X. Han, Y. Yao, C. Wang, Y. Wang, Y. Chen, C. Yan, Y. Li, E.D. Wachsman, L. Hu, *Proc. Natl. Acad. Sci. Unit. States Am.* 113 (2016) 7094.
- [24] C. Wang, H. Zhang, J. Li, J. Chai, S. Dong, G. Cui, *J. Power Sources* 397 (2018) 157–161.
- [25] Y. Zhang, Y. Zhong, Q. Shi, S. Liang, H. Wang, *J. Phys. Chem. C* 122 (2018) 21462–21467.
- [26] J. Motavalli, *Nature* 526 (2015) S96.
- [27] S. Seki, Y. Kobayashi, H. Miyashiro, Y. Mita, T. Iwahori, *Chem. Mater.* 17 (2005) 2041–2045.
- [28] T. Yamanaka, H. Nakagawa, S. Tsubouchi, Y. Domi, T. Doi, T. Abe, Z. Ogumi, *J. Power Sources* 359 (2017) 435–440.
- [29] J.B. Goodenough, Y. Kim, *Chem. Mater.* 22 (2010) 587–603.
- [30] Q. Yang, J. Huang, Y. Li, Y. Wang, J. Qiu, J. Zhang, H. Yu, X. Yu, H. Li, L. Chen, *J. Power Sources* 388 (2018) 65–70.
- [31] J. Ma, Z. Liu, B. Chen, L. Wang, L. Yue, H. Liu, J. Zhang, Z. Liu, G. Cui, *J. Electrochem. Soc.* 164 (2017) A3454–A3461.
- [32] S. Choudhury, Z. Tu, A. Nijamudheen, M.J. Zachman, S. Stalin, Y. Deng, Q. Zhao, D. Vu, L.F. Kourkoutis, J.L. Mendoza-Cortes, L.A. Archer, *Nat. Commun.* 10 (2019) 3091.
- [33] Y. Zhu, Y. Zhang, L. Lu, *J. Power Sources* 290 (2015) 123–129.
- [34] Y. Zhu, X. He, Y. Mo, *ACS Appl. Mater. Interfaces* 7 (2015) 23685–23693.
- [35] J. Zheng, M.H. Engelhard, D. Mei, S. Jiao, B.J. Polzin, J.-G. Zhang, W. Xu, *Nat. Energy* 2 (2017) 17012.
- [36] X. Fan, L. Chen, O. Borodin, X. Ji, J. Chen, S. Hou, T. Deng, J. Zheng, C. Yang, S.-C. Liou, K. Amine, K. Xu, C. Wang, *Nat. Nanotechnol.* 13 (2018) 715–722.
- [37] C. Fang, X. Wang, Y.S. Meng, *Trends Chem.* 1 (2019) 152–158.
- [38] M. Ge, D.S. Coburn, E. Nazaretski, W. Xu, K. Gofron, H. Xu, Z. Yin, W.-K. Lee, *Appl. Phys. Lett.* 113 (2018), 083109.
- [39] R.S. Macomber, *A Complete Introduction to Modern NMR Spectroscopy*, Wiley, New York, NY, 1998.
- [40] W.-S. Yoon, K.-B. Kim, M.-G. Kim, M.-K. Lee, H.-J. Shin, J.-M. Lee, J.-S. Lee, C.-H. Yo, *J. Phys. Chem. B* 106 (2002) 2526–2532.
- [41] C.-H. Chen, B.-J. Hwang, C.-Y. Chen, S.-K. Hu, J.-M. Chen, H.-S. Sheu, J.-F. Lee, *J. Power Sources* 174 (2007) 938–943.